Tunable Electromagnetic Flow Control in Valley Photonic Crystal Waveguides

Xiao-Dong Chen,[1] Fu-Long Shi,[1] Huan Liu,[1] Jin-Cheng Lu,[1] Wei-Min Deng,[1] Jun-Yan Dai,[2] Qiang Cheng,[2,*] and Jian-Wen Dong[1,†]

[1]*School of Physics & State Key Laboratory of Optoelectronic Materials and Technologies, Sun Yat-sen University, Guangzhou 510275, China*

[2]*State Key Laboratory of Millimeter Waves, Southeast University, Nanjing 210096, China*

(Received 9 May 2018; revised manuscript received 25 July 2018; published 1 October 2018)

The exploration of the binary valley degree of freedom in topological photonic systems has inspired many intriguing optical phenomena such as the photonic Hall effect, robust delay lines, and perfect out-coupling refraction. In this work, we experimentally demonstrate the tunability of electromagnetic flow in a valley photonic crystal waveguide. By continuously controlling the phase differences of a microwave monopolar antenna array, the flow of electromagnetic waves can split into different directions according to the chirality of the phase vortex, and the splitting ratio varies from 0.9 to 0.1. Topological valley transport of edge states is also observed at the photonic domain wall. Tunable edge state dispersion, i.e., from gapless valley-dependent modes to gapped flat bands, is found at the photonic boundary between a valley photonic crystal waveguide and a perfect electric conductor, leading to the tunable frequency bandwidth of high transmission. Our work paves the way to the controllable and dynamic modulation of electromagnetic flow in topological photonic systems.

DOI: 10.1103/PhysRevApplied.10.044002

I. INTRODUCTION

Due to the advanced fabrication, numerical modeling, and characterization tools, the flexible manipulation of electromagnetic (em) waves in a desired manner has been theoretically proposed and experimentally realized by the structures and geometries of man-made materials [1–5]. In particular, photonic crystals (PCs) are man-made periodic optical structures with a set of allowed and forbidden frequency bands in which the flow of em waves occurs [6–8]. For example, a super-collimation effect was achieved in PCs with flat eigen-frequency contours [9,10], a cloaking effect was realized in PCs with accidental Dirac cones at the zone center [11,12], and on-chip routing of spin-polarized light was implemented in glide-plane PC slabs [13,14]. In the past few years, inspired by the discovery of topological insulators, topological photonics has attracted much attention as it provides a way to mold the flow of em waves [15–17]. Topological phases with nonzero-gauge fields have been proposed and realized in different photonic systems [18–25] and acoustic systems [26–30]. Due to the macroscopic system sizes of PCs, one-way propagating edge states were achieved in magnetic PCs by breaking the time-reversal symmetry [31,32] and robust edge states against impurities or defects without backscattering were realized in bianisotropic PCs [33,34] or C_6-symmetric PCs [35–37] with strong photonic spin-orbital coupling.

Recently, the binary valley degree of freedom, which characterizes the frequency extrema in momentum space, has been well explored as it has the potential to be used as an information carrier in next generation optoelectronics [38]. It leads to many intriguing phenomena such as chirality-locked beam splitting [39,40], photonic Hall effect [41,42], robust delay lines [43,44], and perfect out-coupling refraction [45]. By achieving local nonzero Berry curvature near K and K′ points at the Brillouin zone corner, recent developments of valley PCs show an alternative way to achieve SOI topological nanophotonic devices [46]. In this work, we experimentally demonstrate tunable em flow in a topological photonic crystal waveguide by employing the valley degree of freedom. Two kinds of tunable behaviors are shown. The em flow at the frequency of bulk states will split into two opposite directions. The splitting rate varies continuously from 0.9 to 0.1 by controlling the phase vortex of the input source. Topological valley transport of edge states is observed at the photonic domain wall. Tunable edge state dispersion, i.e., from gapless valley-dependent modes to gapped flat bands, is found at the photonic boundary between a valley photonic crystal waveguide and a perfect electric conductor, leading to the tunable frequency range of high transmission.

II. VALLEY PHOTONIC CRYSTAL WAVEGUIDE

Let us start by considering a valley photonic crystal (VPC) waveguide [Fig. 1(a)]. It is constructed with two parallel metal plates at the bottom/top and a honeycomb

*qiangcheng@seu.edu.cn
†dongjwen@mail.sysu.edu.cn

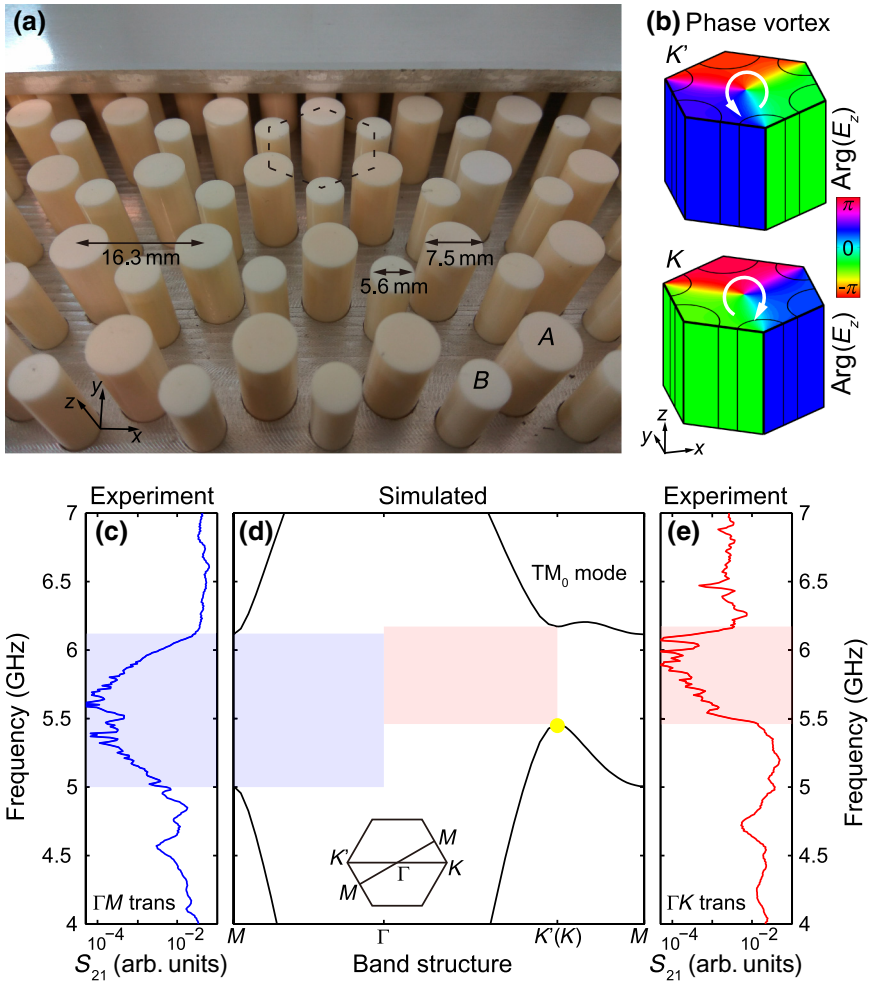

FIG. 1. Experimental sample and bulk band structure of valley photonic crystal waveguide. (a) Photo of the valley photonic crystal waveguide. It has a hexagonal lattice of ceramic rods with the lattice constant of $a = 16.3$ mm. Within a unit cell (black dashed hexagon), there are two kinds of rods with different diameters of 7.5 mm (marked as rod A) and 5.6 mm (rod B), respectively. The rod array is then covered by two parallel metal plates. (b) Valley-contrasting chiral phase distributions of E_z, i.e., arg(E_z), at the frequency of 5.46 GHz for bulk states at K′ and K points [marked by a yellow point in (d)]. (c)–(e) Experimental transmission spectra (c),(e) and calculated bulk band structures (d) of zero-order transverse magnetic waveguide modes (TM$_0$ modes). The directional band gaps along the ΓM and ΓK directions are labeled by blue and pink transparent rectangles, respectively. Inset of (d) shows the Brillouin zone with high symmetry k points. The measured transmission spectra along the (c) ΓM and (e) ΓK directions are used to confirm the frequency range of calculated directional band gaps.

lattice of ceramic rods ($\epsilon = 8.5$) in the middle. The middle ceramic rod array has a lattice constant of $a = 16.3$ mm and a height of 14 mm. The unit cell (outlined by a dashed hexagon) consists of two rods with different diameters, i.e., rod A has a diameter of $d_A = 7.5$ mm while rod B has a diameter of $d_B = 5.6$ mm. The top and bottom metal plates are used to confine em waves along the z direction. By employing the zero-order transverse magnetic waveguide modes (TM$_0$ modes), which are uniform along the z direction, a 3D VPC waveguide is designed to reproduce the band dispersion of TM modes of a 2D VPC. Figure 1(d) shows the simulated lowest bulk band structure of TM$_0$ modes. Directional band gaps along the ΓM and ΓK directions are shaded by blue and pink rectangles, respectively. To prove the simulated directional band gaps, we measure the transmission spectra along the ΓM and ΓK directions, as shown in Figs. 1(c) and 1(e). To enhance the collected signal, we use two horns as the input source and the received detector. The frequency range of the measured transmission dip along the ΓM (ΓK) direction is labeled by the blue (pink) transparent rectangle, showing good agreement with the simulated frequency range of directional band gap. In addition, the first bulk band has a frequency extrema of 5.46 GHz (marked by a yellow point) at the Brillouin zone corners: K′ and K points. These two inequivalent k points are time-reversal partners and hence, the eigen-states at these two k points have different field distributions. To see this, Fig. 1(b) shows the phases of E_z for the K′ valley state (upper panel) and the K valley state (lower panel). Due to the uniformity of the TM$_0$ modes, the E_z phase does not change along the z direction. For the K′ valley state, the E_z phase has a circular phase vortex which decreases counterclockwise by 2π around the center of the unit cell, and we denote it as a left-hand circular polarization (LCP) phase vortex. In contrast, for the K valley state, the E_z phase decreases clockwise by 2π around the center of the unit cell, and we denote it as a right-hand circular polarization (RCP) phase vortex.

III. TUNABLE EXCITATION OF VALLEY BULK STATES

By using the valley dependence of the chiral phase vortex of K′ and K valley states, we can achieve unidirectional excitation and/or tunable excitation of bulk states. The top view of the experimental sample without the top metal

plate is shown in Fig. 2(a). Above the bottom metal plate, there is a bulk VPC (green dashed hexagon), a surrounding piece of plexiglass (red dashed hexagon), and the outmost air background (blue dashed hexagon). Here, plexiglass with a refractive index of 1.5 is used to compensate the parallel momentum and efficiently guide the bulk state outside the VPC. To construct a source with a phase vortex, three monopoles (numbered as 1, 2, and 3 in the inset) are put at the center of the sample. These three monopoles are set with the same amplitudes, but with different initial phases (i.e., φ_1, φ_2, φ_3) by a three-port power divider and three phase shifters. By achieving different combinations of (φ_1, φ_2, φ_3), the input source with different phase vortices can be generated. For example, when $\varphi_1 = 240°$, $\varphi_2 = 120°$, and $\varphi_3 = 0°$, the LCP phase vortex with counterclockwise decreasing phases will be generated [inset of Fig. 2(b)]. By putting such a source with a LCP phase vortex at the center of the VPC, only the K′ valley state can be excited at the working frequency of 5.46 GHz [Fig. 2(b)]. At each boundary, the K′ valley state is partially reflected back into the VPC and partially refracted into the surrounding plexiglass. The refracted em waves are enhanced at the left, upper-right, and lower-right corners of the whole sample. In contrast, when the input source carries another configuration of $\varphi_1 = 0°$, $\varphi_2 = 120°$, $\varphi_3 = 240°$ (i.e., RCP phase vortex source), only the K valley state will be excited, and the refracted em waves will switch to be enhanced at the right, upper-left, and lower-left corners of the whole sample. To quantitatively demonstrate such chiral-source dependent splitting behaviors, we measure the magnitude of E_z fields at the left and right exits, as outlined by two white frames. Meanwhile, we continuously change the phase vortex source from LCP to linear polarization and RCP in order to investigate the splitting behaviors. In the experiment, we keep φ_2 as 120°, but decrease φ_1 from 240° to 0° and increase φ_3 from 0° to 240°. The phase vortex source and VPC waveguide are put on the bottom metal plate, which is stationary during the measurement. The top metal plate is mounted on a two-dimensional motorized translation stage (LINBOU NFS03). A hole is drilled in the top plate and a monopole antenna is inserted to record the electric fields, which will be collected by the vector network analyzer (Agilent E5071C). The measured results near the left and right exits are summarized in Fig. 2(d). The corresponding simulation results are also shown in Fig. 2(c). Here, we list the near-field distributions of five different phase configurations. When the excited source has a LCP phase vortex, i.e., $\varphi_1 = 240°$, $\varphi_2 = 120°$, $\varphi_3 = 0°$ of the first case, E_z fields at the left exit are much larger than those at the right exit, confirming the unidirectional excitation of photonic states in the topological photonic crystal by the chiral source. By decreasing φ_1 while simultaneously increasing φ_3, we measure the output near-field distributions for the other four cases. One can see that both simulated and measured magnitudes at

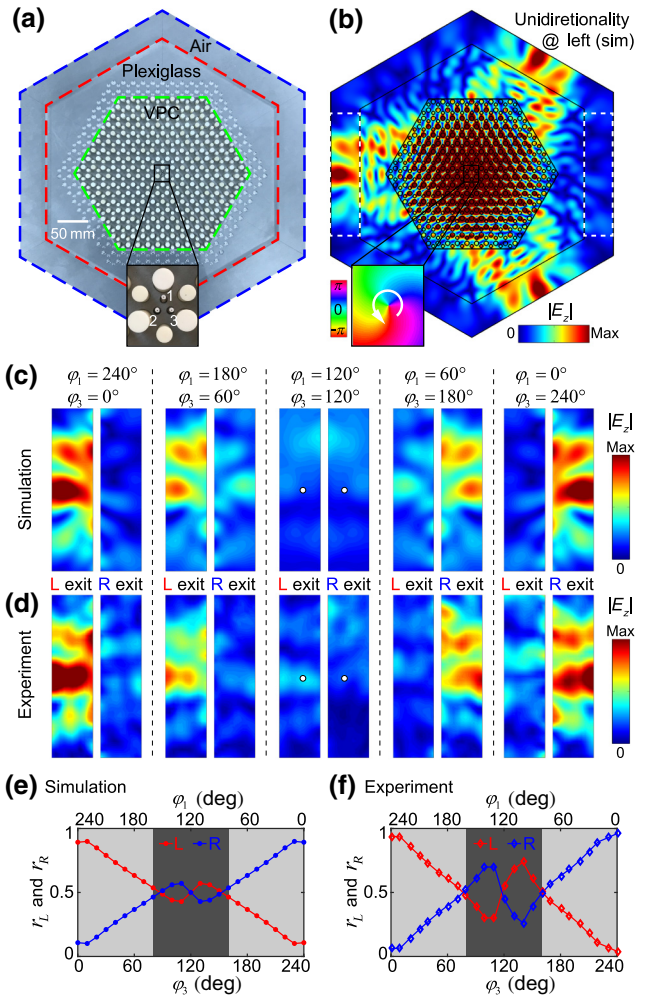

FIG. 2. Tunable excitation of bulk states. (a) Photo of the bulk valley photonic crystal (VPC) waveguide with the removal of the top metal plate to show the inside. Between the top and bottom metal plates, there is a honeycomb lattice of ceramic rods (green dashed hexagon), a piece of plexiglass with a refractive index of 1.5 (red dashed hexagon), and the outmost air background (blue dashed hexagon). Inset: A self-made source is constructed by three monopoles (labeled as 1, 2, and 3) with different initial phases (i.e., φ_1, φ_2, φ_3). (b) Simulated magnitude of E_z when the VPC waveguide is excited by a source with a LCP phase vortex at the frequency of 5.46 GHz. Two white frames outline the regions where E_z are measured. Inset: The phase vortex with counterclockwise decreasing phases is generated when $\varphi_1 = 240°$, $\varphi_2 = 120°$, and $\varphi_3 = 0°$ is input. (c) Simulated and (d) measured magnitudes of E_z at the left and right exits of the bulk sample when φ_2 is kept as 120°, but φ_1 and φ_3 are changed. (e) Simulated and (f) measured splitting ratios of electric fields at the left and right exits. Here, E_z at 20 mm away from the boundary [marked by white dots in (c) and (d)] are chosen to be the representative electric fields. The range of φ_1 from 160° to 80° (shaded in dark gray) is out of the discussed scope as the corresponding electric fields at the left and right exits are too small. The splitting ratio from 0.9 to 0.1 can be achieved when φ_1 ranges from 240° to 170° and 70° to 0°.

the left exit gradually become smaller while those at the right exit become larger when the input source changes. To characterize the tunable output field distribution, we focus on E_z at 20 mm away from the boundary between the plexiglass and air [marked by white dots in the third case of Figs. 2(c) and 2(d)]. We define $r_L = |E_z^L|/(|E_z^L| + |E_z^R|)$ and $r_R = |E_z^R|/(|E_z^L| + |E_z^R|)$ to show the splitting ratios of the field magnitudes at the left and right exits. As shown in Fig. 2(e), the splitting ratio (red curve) at the left exit r_L is 0.9 for the LCP phase vortex source. It gradually becomes smaller along with the decreasing φ_1 (while increasing φ_3), and at last reaches 0.1 when the source has a RCP phase vortex. The measured experimental splitting ratios r_L and r_R are in good agreement with the simulated results. Note that there is a mismatch between simulated and experimental results when φ_1 ranges from 160° to 80° [dark gray region in Figs. 2(e) and 2(f)]. This is because the electric fields have a small magnitude, e.g., the third column in Figs. 2(c) and 2(d), leading to a relatively large signal-noise ratio error. For the practical applications, one may focus on the ranges of φ_1 from 240° to 170° and from 70° to 0° [light gray in Figs. 2(e) and 2(f)] to achieve a splitting ratio of the electric fields from 0.9 to 0.1. Note that the splitting of em waves is important in applications such as splitters, demultiplexers, modulators, and interferometers. In contrast to other beam splitters that employ the frequency or polarization of em waves, the splitter in this work exploits the phase of em waves and a tunable splitting ratio is achieved by changing the input phases.

IV. ROBUST TRANSPORT OF VALLEY EDGE STATES

Besides the valley-dependent phase vortex, the VPC waveguide has a valley-dependent Berry curvature [47]. This leads to another important property of the VPC waveguide, i.e., the robust transport of edge states of the photonic domain wall. Figure 3(a) shows the top view of the photonic domain wall. The VPC waveguide presented in Fig. 1(a) [denoted as VPC1] and its inverted one [denoted as VPC2] locate above and below the domain wall, respectively. Previous theoretical results indicate that the topological indices of VPC1 (VPC2) are $C_{\mathrm{K}'} = +1/2$ and $C_{\mathrm{K}} = -1/2$ ($C_{\mathrm{K}'} = -1/2$ and $C_{\mathrm{K}} = +1/2$) [47]. Across the boundary, the differences of the topological indices are -1 and $+1$ at the K′ and K valleys, respectively. According to the bulk edge correspondence, there will be one edge state with a negative (positive) group velocity at the K′ (K) valley, which is confirmed by the numerical edge dispersion shown in Fig. 3(b). When the intervalley scattering is prohibited, robust transport of these valley-dependent edge states can be observed. To see this, we construct two different photonic boundaries, i.e., the flat channel and a Z-shaped bend [Figs. 3(d) and 3(e)]. Here, the top metal plate is removed to show the boundary morphology inside (outlined by the blue and red dashed lines). Figure 3(c) shows the measured transmission spectra for both a flat channel (blue line) and the Z-shaped bend (red line). Within the frequency range of edge states [shaded by a blue transparent rectangle], high transmission is preserved even when the excited edge states go along the Z-shaped bend with two sharp corners. To directly image the robust transmission, we also scan the transmitted E_z fields [Figs. 3(f) and 3(g)]. In the experiment, the edge states are excited by a monopole located at the left entrance of two boundaries. From the E_z magnitudes shown in Figs. 3(f) and 3(g), we can directly see the edge states pass along the Z-shaped bend without scattering and the robust transport of valley edge states is demonstrated.

The above-mentioned valley-dependent edge states are achieved at the domain wall between two VPCs with distinct topologies. Next, we show that such valley-dependent edge states can also be obtained at the boundary between only one VPC waveguide and another homogeneous insulator [Fig. 4]. Considering the domain wall in Fig. 3(a), we replace the upper VPC1 waveguide with a perfect magnetic conductor (PMC) [Fig. 4(a)]. Figure 4(b) shows corresponding edge states dispersion, which is the same as the edge states dispersion of the domain wall in Fig. 3(b). Comparing to the domain wall, the simplified PMC-capped VPC waveguide can reduce the sample size by half. Note that the PMC is typically realized by artificial resonant structures with narrow operating bands, and we then discuss the boundary between the VPC waveguide and the perfect electric conductor (PEC) [left schematic of Fig. 4(d)]. The distance between the PEC and the nearest rod (highlighted in red) is set to be 4 mm. To obtain edge states whose frequency range covers the complete band gap, we tune the diameter of the nearest rods to be $d = 5.5$ mm. Figure 4(e) shows the gapless edge dispersion of this boundary. The edge states with a positive group velocity appear at the K′ valley while the edge states have a negative group velocity at the K valley. In searching for the origin of these valley-dependent edge states, we notice that similar gapless edge states also exist at the topological domain wall of two VPCs [right schematic of Fig. 4(d)]. Considering the odd modes of the domain wall, the electric fields are required to be perpendicular to the mirror symmetric plane (black dashed line), as if an effective PEC boundary were there. Therefore, solving the odd modes of the topological domain wall of two VPCs [right schematic of Fig. 4(d)] is equivalent to solving the eigenmodes of the edge states of PEC-capped VPCs [left schematic of Fig. 4(d)]. However, compared to the domain wall, the simplified PEC-capped VPC waveguide can reduce the sample size by half. The edge states can evolve continuously from the gapless valley-dependent modes to the flat band by tuning the magnitude of the photonic potential near the boundary, when the topological property of

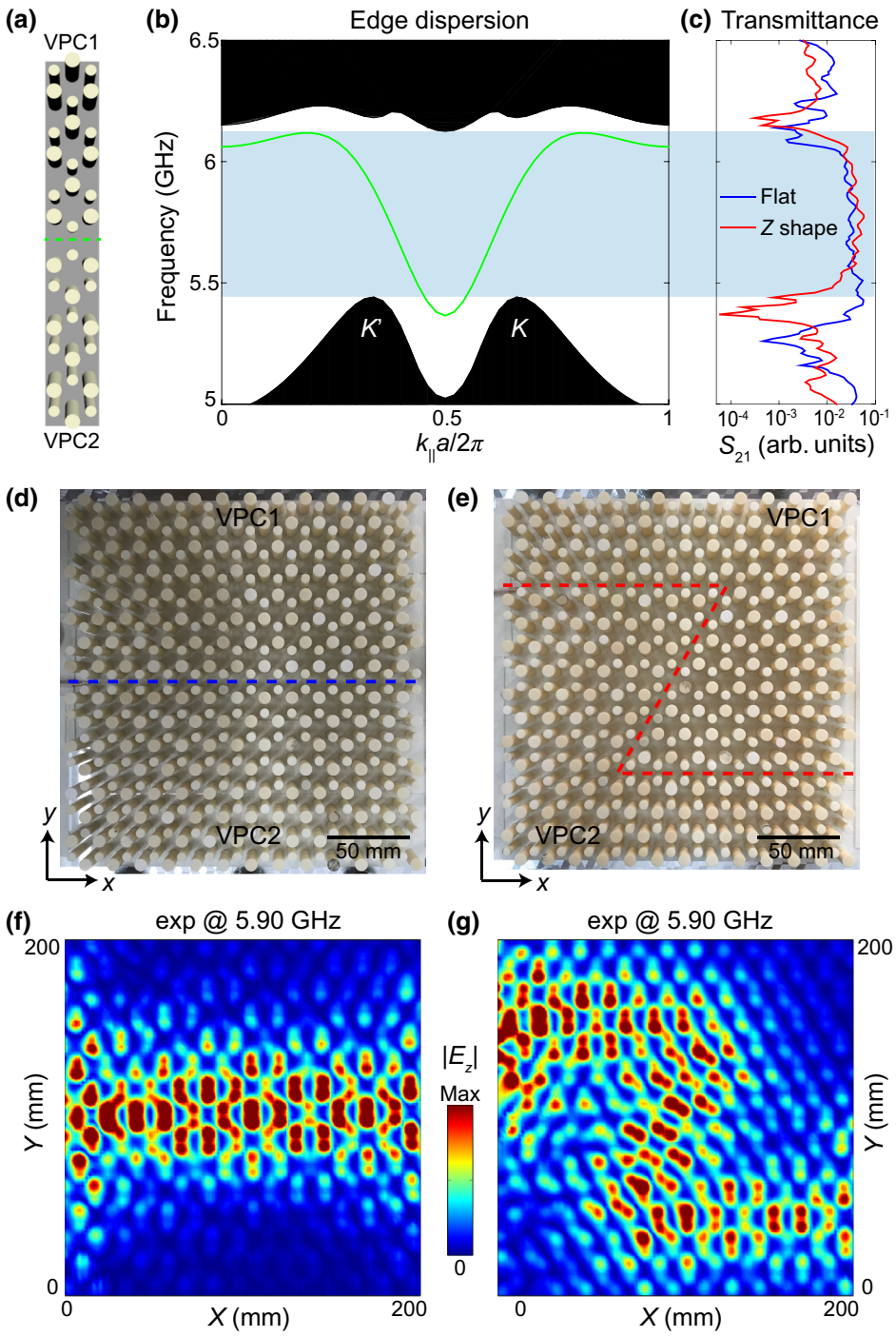

FIG. 3. Observation of broadband robust transport of valley edge states. (a) Schematic of photonic boundary between two topologically-distinct valley photonic crystals (VPC1 and VPC2). (b) Edge dispersion corresponding to the boundary in (a). The green line represents the edge states and the black region corresponds to the projection bulk bands. (c) Measured transmission spectra of the flat channel (blue curve) and the Z-shaped bend (red curve). The complete band gap is labeled in both (b) and (c) by a blue transparent rectangle. (d),(e) Photos of (d) the flat channel and (e) the Z-shaped bend between VPC1 and VPC2. The interface is outlined by the blue and red dashed lines, respectively. (f),(g) Measured magnitude of E_z for (f) the flat channel and (g) the Z-shaped bend at the frequency of 5.9 GHz.

bulk VPC is unchanged. To see this, we increase the photonic potential by enlarging the diameter of the nearest rods from $d = 5.5$ mm to $d = 6.5$ mm [Fig. 4(f)] and to $d = 7.5$ mm [Fig. 4(g)]. When the diameters of the nearest rods become larger, more energy of edge states locates at the ceramic rods with high permittivity, and the edge dispersions are shifted to a lower frequency, achieving the evolution from gapless edge states to flat dispersion bands. In addition, the frequency range of edge states is easily tuned by changing the diameters of the ceramic rods, serving as a platform for realizing tunable frequency bandwidth with high transmission. We also simulate the transmission spectra of the tunable edge states of PEC-capped VPC [Fig. 4(h)]. The source is incident from the left and the transmission is recorded at the right end of the boundary. Figure 4(i) illustrates the high transmission in the complete band gap frequency range when $d = 5.5$ mm [red curve]. When d is changed to 6.5 mm, transmission near 6 GHz

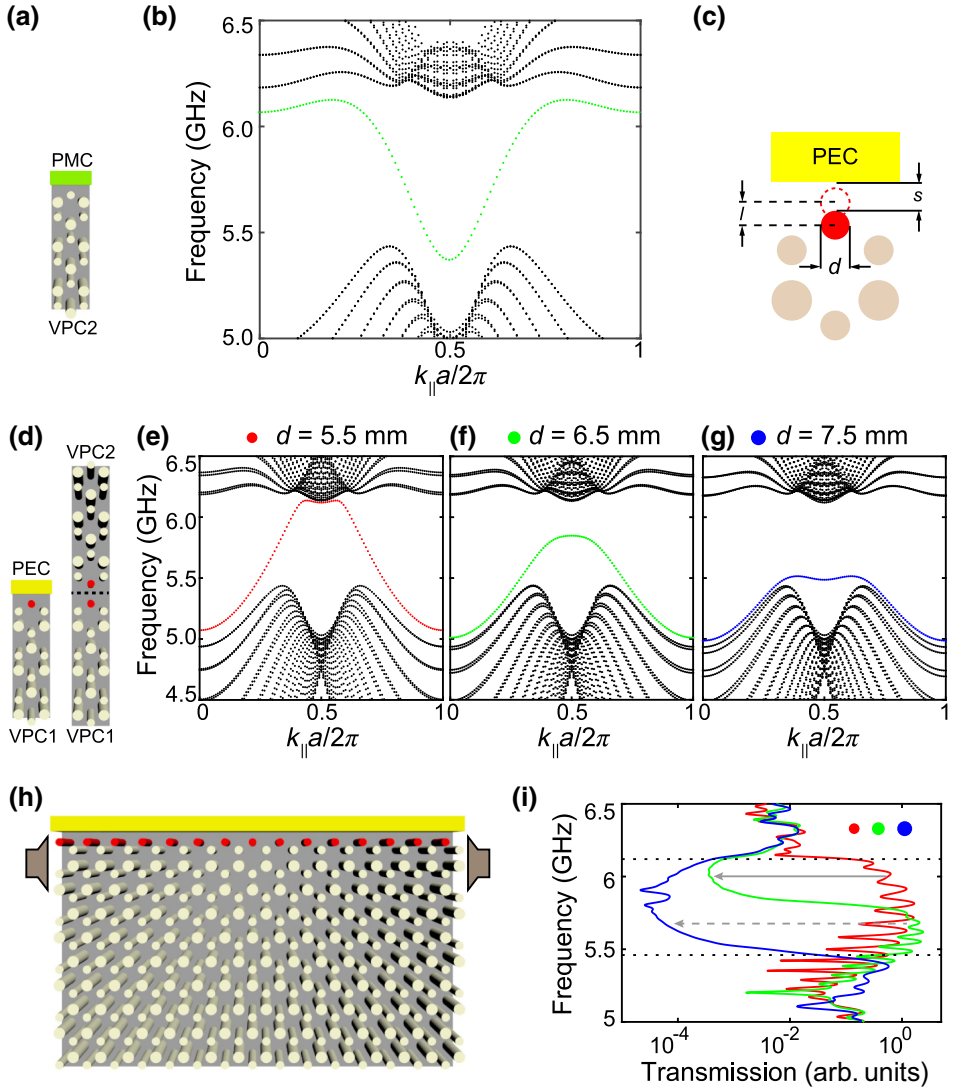

FIG. 4. Tunable edge dispersion from gapless valley-dependent modes to gapped flat band. (a) Schematic of the boundary between a VPC2 waveguide and a PMC. (b) Edge state dispersion for photonic boundary in (a). (c) The 2D (*x*-*y* plane) view of the schematic of a PEC-capped VPC waveguide. Tunable edge dispersion can be achieved by changing the position of rods (*l*), the distance between PEC and the nearest rods (*s*), or the diameter of the nearest rods (*d*). (d) Schematics of the boundary between the VPC1 waveguide and a PEC (left) and the topological domain wall between two VPC waveguides (right). (e)–(g) Edge state dispersion for photonic boundary with nearest ceramic rods having diameters of (b) $d = 5.5$ mm, (c) $d = 6.5$ mm, and (d) $d = 7.5$ mm. Here, the distance between the center of the nearest rod and PEC is 4 mm. The evolution from gapless valley-dependent modes to gapped flat band are observed. (h) Schematic of the photonic boundary for tunable high transmission. Source is incident from the left and the transmission is recorded at the right. (i) Transmission spectra of tunable frequency range of high transmission. Solid gray arrow (gray dashed arrow) marks that the transmission at 6 GHz (5.7 GHz) drops when the rod diameter is changed to $d = 6.5$ mm ($d = 7.5$ mm). Two black dashed lines mark the frequency range of the complete band gap.

drops [gray solid arrow] while it remains unchanged near 5.7 GHz. When *d* is further enlarged to 7.5 mm, transmission at 5.7 GHz drops [gray dashed arrow]. Therefore, tunable high transmission of edge states can be achieved by increasing the rod diameter. Note that similar tunable edge state dispersion and tunable high transmission can also be realized by changing the distance between rods and PEC (*s*) or by changing the positions of the rods (*l*) [Fig. 4(c)]. For example, consider the PEC-capped VPC waveguide with fixed $d = 7.5$ mm, but varying *s*. Gapless edge states can be obtained when $s = 0$ mm and gapped flat bands are achieved when $s = 3$ mm.

V. CONCLUSION

In conclusion, we design and fabricate a VPC waveguide by sandwiching a honeycomb lattice of ceramic rods between two parallel metal plates. Using the phase vortex

of valley bulk states, a tunable flow of em waves is experimentally achieved in such a VPC waveguide. The flow of em waves splits into different directions and the splitting ratio can continuously vary from 0.9 to 0.1. Furthermore, at the topological domain wall between two distinct VPC waveguides, robust transport of edge states is observed. In addition, we demonstrate tunable edge state dispersion, i.e., from gapless valley-dependent modes to gapped flat bands, at the photonic boundary between a VPC waveguide and a PEC, leading to the feasibility of manipulating the frequency range of high transmission.

ACKNOWLEDGMENTS

This work is supported by Natural Science Foundation of China (Grants No. 11704422, No. 61775243, and No. 11522437), and Fundamental Research Funds for the Central Universities (Grant No. 17lgpy19).

X.-D.C. and F.-L.S. contributed equally to this work.

[1] S. Jahani and Z. Jacob, All-dielectric metamaterials, Nat. Nanotechnol. **11**, 23 (2016).

[2] W. Gao, M. Lawrence, B. Yang, F. Liu, F. Fang, B. Béri, J. Li, and S. Zhang, Topological Photonic Phase in Chiral Hyperbolic Metamaterials, Phys. Rev. Lett. **114**, 037402 (2015).

[3] N. Yu, P. Genevet, M. A. Kats, F. Aieta, J.-P. Tetienne, F. Capasso, and Z. Gaburro, Light propagation with phase discontinuities: Eneralized laws of reflection and refraction, Science **334**, 333 (2011).

[4] C. Pfeiffer and A. Grbic, Bianisotropic Metasurfaces for Optimal Polarization Control: Analysis and Synthesis, Phys. Rev. Appl. **2**, 044011 (2014).

[5] P. Qiao, W. Yang, and C. J. Chang-Hasnain, Recent advances in high-contrast metastructures, metasurfaces, and photonic crystals, Adv. Opt. Photonics **10**, 180 (2018).

[6] J. D. Joannopoulos, S. G. Johnson, J. N. Winn, and R. D. Meade, *Photonic Crystals - Molding the Flow of Light* (Princeton University Press, Princeton, NJ, 2008).

[7] K. Sakoda, *Optical Properties of Photonic Crystals* (Springer Science & Business Media, New York, 2005).

[8] Y. Yang, X. Huang, and Z. H. Hang, Experimental Characterization of the Deterministic Interface States in Two-Dimensional Photonic Crystals, Phys. Rev. Appl. **5**, 034009 (2016).

[9] H. Kosaka, T. Kawashima, A. Tomita, M. Notomi, T. Tamamura, T. Sato, and S. Kawakami, Photonic crystals for micro lightwave circuits using wavelength-dependent angular beam steering, Appl. Phys. Lett. **74**, 1370 (1999).

[10] W. Y. Liang, J. W. Dong, and H. Z. Wang, Directional emitter and beam splitters based on self-collimation effect, Opt. Express **5**, 1234 (2007).

[11] X. Huang, Y. Lai, Z. H. Hang, H. Zheng, and C. T. Chan, Dirac cones induced by accidental degeneracy in photonic crystals and zero-refractive-index materials, Nat. Mater. **10**, 582 (2011).

[12] J.-W. Dong, M.-L. Chang, X.-Q. Huang, Z. H. Hang, Z.-C. Zhong, W.-J. Chen, Z.-Y. Huang, and C. T. Chan, Conical Dispersion and Effective Zero Refractive Index in Photonic Quasicrystals, Phys. Rev. Lett. **114**, 163901 (2015).

[13] I. Söllner, S. Mahmoodian, S. L. Hansen, L. Midolo, A. Javadi, G. Kiršanskė, T. Pregnolato, H. El-Ella, E. H. Lee, J. D. Song, S. Stobbe, and P. Lodahl, Deterministic photon-emitter coupling in chiral photonic circuits, Nat. Nanotechnol. **10**, 775 (2015).

[14] P. Lodahl, S. Mahmoodian, S. Stobbe, A. Rauschenbeutel, P. Schneeweiss, J. Volz, H. Pichler, and P. Zoller, Chiral quantum optics, Nature **541**, 473 (2017).

[15] L. Lu, J. D. Joannopoulos, and M. Soljačić, Topological photonics, Nat. Photonics **8**, 821 (2014).

[16] C. He, L. Lin, X.-C. Sun, X.-P. Liu, M.-H. Lu, and Y.-F. Chen, Topological photonic states, Int. J. Mod. Phys. B **28**, 1441001 (2013).

[17] Y. Wu, C. Li, X. Hu, Y. Ao, Y. Zhao, and Q. Gong, Applications of topological photonics in integrated photonic devices, Adv. Opt. Mater. **5**, 1700357 (2017).

[18] M. Xiao, Z. Q. Zhang, and C. T. Chan, Surface Impedance and Bulk Band Geometric Phases in One-Dimensional Systems, Phys. Rev. X **4**, 021017 (2014).

[19] Q. Wang, M. Xiao, H. Liu, S. Zhu, and C. T. Chan, Measurement of the Zak phase of photonic bands through the interface states of a metasurface/photonic crystal, Phys. Rev. B **93**, 041415 (2016).

[20] L. Lu, Z. Wang, D. Ye, L. Ran, L. Fu, J. D. Joannopoulos, and M. Soljačić, Experimental observation of Weyl points, Science **349**, 622 (2015).

[21] M. Xiao, W. Chen, W. He, and C. T. Chan, Synthetic gauge flux and Weyl points in acoustic systems, Nat. Phys. **11**, 920 (2015).

[22] M. C. Rechtsman, J. M. Zeuner, Y. Plotnik, Y. Lumer, D. Podolsky, F. Dreisow, S. Nolte, M. Segev, and A. Szameit, Photonic Floquet topological insulators, Nature **496**, 196 (2013).

[23] M. Hafezi, E. A. Demler, M. D. Lukin, and J. M. Taylor, Robust optical delay lines with topological protection, Nat. Phys. **7**, 907 (2011).

[24] V. Peano, C. Brendel, M. Schmidt, and F. Marquardt, Topological Phases of Sound and Light, Phys. Rev. X **5**, 031011 (2015).

[25] Z.-G. Chen and Y. Wu, Tunable Topological Phononic Crystals, Phys. Rev. Appl. **5**, 054021 (2016).

[26] C. He, X. Ni, H. Ge, X.-C. Sun, Y.-B. Chen, M.-H. Lu, X.-P. Liu, and Y.-F. Chen, Acoustic topological insulator and robust one-way sound transport, Nat. Phys. **12**, 1124 (2016).

[27] Q. Wei, Y. Tian, S.-Y. Zuo, Y. Cheng, and X.-J. Liu, Experimental demonstration of topologically protected efficient sound propagation in an acoustic waveguide network, Phys. Rev. B **95**, 094305 (2017).

[28] Y. G. Peng, C. Z. Qin, D. G. Zhao, Y. X. Shen, X. Y. Xu, M. Bao, H. Jia, and X. F. Zhu, Experimental demonstration of anomalous Floquet topological insulator for sound, Nat. Commun. **7**, 13368 (2016).

[29] Y.-G. Peng, Y.-X. Shen, D.-G. Zhao, and X.-F. Zhu, Low-loss and broadband anomalous Floquet topological insulator for airborne sound, Appl. Phys. Lett. **110**, 173505 (2017).

[30] Y.-G. Peng, Z.-G. Geng, and X.-F. Zhu, Topologically protected bound states in one-dimensional Floquet acoustic waveguide systems, J. Appl. Phys. **123**, 091716 (2018).
[31] Y. Poo, R.-x. Wu, Z. Lin, Y. Yang, and C. T. Chan, Experimental Realization of Self-Guiding Unidirectional Electromagnetic Edge States, Phys. Rev. Lett. **106**, 093903 (2011).
[32] S. Liu, J. Du, Z. Lin, R. Wu, and S. Chui, Formation of robust and completely tunable resonant photonic band gaps, Phys. Rev. B **78**, 155101 (2008).
[33] T. Ma and G. Shvets, Scattering-free edge states between heterogeneous photonic topological insulators, Phys. Rev. B **95**, 165102 (2017).
[34] X. Cheng, C. Jouvaud, X. Ni, S. H. Mousavi, A. Z. Genack, and A. B. Khanikaev, Robust reconfigurable electromagnetic pathways within a photonic topological insulators, Nat. Mater. **15**, 542 (2016).
[35] L.-H. Wu and X. Hu, Scheme for Achieving a Topological Photonic Crystal by Using Dielectric Material, Phys. Rev. Lett. **114**, 223901 (2015).
[36] Y. Yang, Y. F. Xu, T. Xu, H.-X. Wang, J.-H. Jiang, X. Hu, and Z. H. Hang, Visualization of a Unidirectional Electromagnetic Waveguide Using Topological Photonic Crystals Made of Dielectric Materials, Phys. Rev. Lett. **120**, 217401 (2018).
[37] S. Barik, H. Miyake, W. DeGottardi, E. Waks, and M. Hafezi, Two-dimensionally confined topological edge states in photonic crystals, New J. Phys. **18**, 113013 (2016).
[38] X. Xu, W. Yao, D. Xiao, and T. F. Heinz, Spin and pseudospins in layered transition metal dichalcogenides, Nat. Phys. **10**, 343 (2014).
[39] L. Ye, C. Qiu, J. Lu, X. Wen, Y. Shen, M. Ke, F. Zhang, and Z. Liu, Observation of acoustic valley vortex states and valley-chirality locked beam splitting, Phys. Rev. B **95**, 174106 (2017).
[40] J. Lu, C. Qiu, W. Deng, X. Huang, F. Li, F. Zhang, S. Chen, and Z. Liu, Valley Topological Phases in Bilayer Sonic Crystals, Phys. Rev. Lett. **120**, 116802 (2018).
[41] J.-W. Dong, X.-D. Chen, H. Zhu, Y. Wang, and X. Zhang, Valley photonic crystals for control of spin and topology, Nat. Mater. **16**, 298 (2017).
[42] Z. Gao, Z. Yang, F. Gao, H. Xue, Y. Yang, J. Dong, and B. Zhang, Valley surface-wave photonic crystal and its bulk/edge transport, Phys. Rev. B **96**, 201402 (2017).
[43] T. Ma and G. Shvets, All-si valley-Hall photonic topological insulator, New J. Phys. **18**, 025012 (2016).
[44] Z. Zhang, Y. Tian, Y. Cheng, Q. Wei, X. Liu, and J. Christensen, Topological Acoustic Delay Line, Phys. Rev. Appl. **9**, 034032 (2018).
[45] F. Gao, H. Xue, Z. Yang, K. Lai, Y. Yu, X. Lin, Y. Chong, G. Shvets, and B. Zhang, Topologically protected refraction of robust kink states in valley photonic crystals, Nat. Phys. **14**, 140 (2017).
[46] M. I. Shalaev, W. Walasik, A. Tsukernik, Y. Xu, and N. M. Litchinitser, Experimental demonstration of valley-Hall topological photonic crystal at telecommunication wavelengths, arXiv:1712.07284.
[47] X.-D. Chen, F.-L. Zhao, M. Chen, and J.-W. Dong, Valley-contrasting physics in all-dielectric photonic crystals: Orbital angular momentum and topological propagation, Phys. Rev. B **96**, 020202(R) (2017).